Experimental study of the dimensionless wavenumber of capillary waves on semi-infinite liquid jets

Bachelor thesis by

Niels van der Vlugt
&
Maurits Verkerke

July 2012

Bachelor Applied Physics
Research department Physics of Fluids
Faculty of Science and Technology
University of Twente

Tutors: MSc. T. Driessen and
MSc. M.P. van der Meulen
Teacher: Prof. Dr. Detlef Lohse

Abstract

In this thesis capillary waves that are emitted by tail drops of semi-infinite liquid jets are investigated analytically and experimentally. The dimensionless wavenumber of these capillary waves is determined to try to gain a better insight into one of the effects leading to pinch off. Using a single flash approach and an iLIF[1] set-up several shapes of microdrops are investigated.

After determining the dispersion relation of the capillary waves a theoretical expectation value of $\kappa = \sqrt{3}$ is obtained. This expectation value is approached in more stable drops, jetted with lower jetting voltages (110 V). The dimensionless wavenumber however decreases for drops jetted with higher voltages (118 V), suggesting that the dimensionless wavenumber is not constant for all drops. In a second approach the expectation value is set as a function of the capillary wave speed and a theoretical capillary speed. This results in an even bigger deviation, from which can be concluded that the theoretical basis used in these experiments does not suffice to describe the capillary waves on the liquid jets generated in these experiments.

Table of contents

List of symbols

κ	dimensionless wavenumber
$E_{surface}$	surface energy
γ	surface tension
A	surface area of liquid jet
dE	change in energy
R	radius of ligament
z	radial coordinate of ligament
φ	azimuthal angle
R_0	jet radius of unperturbed ligament
ϵ	amplitude of perturbations
k	longitudinal wavenumber
m	azimuthal wavenumber
ω	growth rate of perturbations
ρ	density
I_1	first order Bessel function
I_0	zeroth order Bessel function
U_{cw}	speed of capillary waves
t_{cap}	capillary time scale
U_{cap}	capillary speed
F_{line}	line tension
$F_{Laplace}$	Laplace force
$\Phi_{momentum}$	momentum flux
u	speed of fluid in liquid jet
U	speed of object captured by camera
U_{pix}	speed of object captured by camera in pix/s
M_{eff}	effective magnification
d	pixel size
ε	displacement of the object
t	exposure time
λ	wavelength of capillary wave
V	volume
Δx	width of disk
Φ_{vol}	volume flux
V_{td}	volume of tail drop
U_{td}	speed of tail drop relative to liquid jet
A_{in}	surface area through which liquid enters the tail drop
κ_2	second approximation of the dimensionless wave number

1 Introduction

Printing nowadays can be done in a number of ways, of which laser printing and ink jet printing are probably the two most well known. Although laser printing was very popular at the beginning of this century, a lot of applications that might grow big in the future, will have their roots in ink jet printing. One can for example think of large one of a kind prints and printing of solar cells[2].

In inkjet printing ink is ejected from a nozzle. To leave the nozzle, the ink must reach a certain speed. Since it takes a certain amount of time for the liquid to break from the nozzle, the ink stretches out into a long ligament with a main drop in front and a smaller tail drop at the end. For optimal print quality however a single spherical drop is desirable. Unfortunately the ligament often breaks up small satellites before contracting to a spherical drop due to the Rayleigh-Plateau instability[3]. Before breaking up capillary waves can be seen to propagate in front of the tail drop. These capillary waves grow over time which will result in pinch off of the tail drop from the ligament. Three different stages of a propagating droplet can be found in figure 1. The stability of these liquid ligaments has not yet been fully understood and is a subject of great interest in studies on ink jet printing.

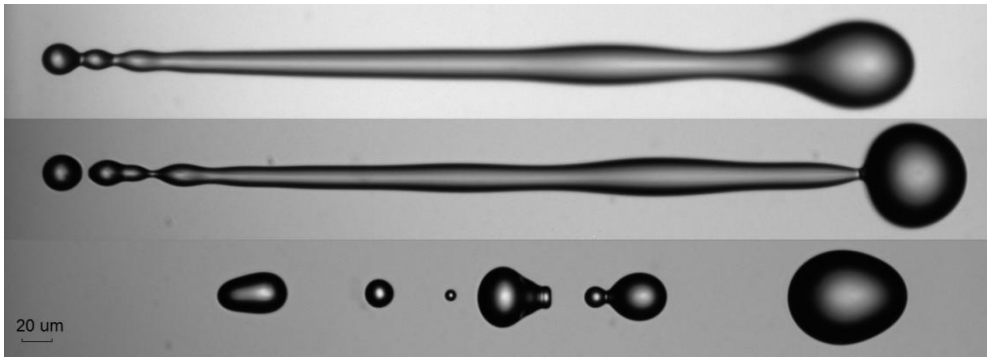

Figure 1: Three different stages of a propagating droplet (not the same droplets), originating from a nozzle at the left side, which is not on the image. Above: intact droplet. Middle: pinch off at the droplet. Below: droplet broken up.

The main focus of this thesis will be on the before mentioned capillary waves, to try to gain a better insight into one of the effects leading to pinch off. Two different models will be used to make a prediction about their dimensionless wavenumber (κ), which is found by multiplying the mean local radius of the jet by the wavenumber. First, with a simple model using a dispersion relation describing how the growth rate of the capillary waves depends on their wavenumber a rough estimate can be made. For this a jet impinging on a liquid reservoir is considered, from which a set of assumptions can be made leading to a constant value $\kappa = \sqrt{3}$. The second model includes the tail drop on the end of the ligament and builds on the dispersion relation by including a force balance between the tail drop and the ligament.

Experiments with a microdrop dispenser using a piezo electric actuator are done at different jetting voltages, thereby not only varying the speed of the liquid but the radius of the ligament and the length of the total droplets as well. It is found the first approximation holds better for lower jet speeds. The second model does not seem to result in a better prediction than the first no matter what the jet speed is.

The experimental part of this paper involves capturing fast moving micro scale fluid motions, hence a fast camera or a short illumination time with an intense light source is needed. The experiments done for this paper make use of a relatively new technique called laser-induced fluorescence (iLIF)[1]. This technique uses a Q-switched Nd:YAG laser ($\lambda = 1064$nm) and a fluorescent plate to produce 7 nanosecond, low-coherent pulses of light to illuminate liquid droplets. The spectrum of the iLIF light lies between 600 and 800 nm. Because droplets jetted by a piezoelectric microdrop are of high reproducibility no high speed camera is needed. Single flash stroboscopy can be used instead. Using the iLIF light source, a 'simple' 1 Hz camera, a BNC pulse/delay generator and a microdrop system it is possible to produce high quality and high contrast, motion blur free images of fast moving liquid droplets. This makes it possible to study the capillary waves in detail.

2 Theory

Breakup of liquid jets has already been described in the end of the 19th century. In 1879 Lord Rayleigh proved[3] that breakup is caused by a pressure discontinuity due to surface tension, after Joseph Plateau in 1873 found[4] that jets break up if the length of the jet exceeds its circumference. This concept is known as the Rayleigh-Plateau instability.

2.1 Rayleigh-Plateau instability

The Rayleigh-Plateau instability on a falling jet can be seen as way for the system to evolve to a more favourable energy state. The surface energy of a jet

$$E_{surface} = \gamma A \qquad \text{[eq. 1]}$$

In which A is the surface area of the jet and γ the surface tension, where the latter is a constant. This means $dE = \gamma dA$ must also hold and changes in surface area will lead to a change in surface energy.
From this the question arises if any deformation of the jet at constant volume, thereby changing the surface area, will result in a net lower surface energy. If so, small perturbations or noise will allow such a system to go to a lower energy state.
Two deformations of the jet can now be thought of, the first being sinusoidal undulations of the jet centerline and the second modulations of the jet radius. The former will have no effect on the net surface area[5] if the radius remains constant. The latter may change its surface energy though. A perturbation of the jet radius can be written as

$$R(z,\varphi) = R_0 + \epsilon \cos(kz)\cos(m\varphi) \qquad \text{[eq. 2]}$$

with k the longitudinal wave number and φ the azimuthal angle. It can now be shown[3] that dE relative to the jets initial energy state is

$$\frac{dE}{E_0} = \frac{\epsilon^2}{4R_0^2}[(kR_0)^2 - 1] \qquad \text{[eq. 3]}$$

From which can be concluded that all modes with wavelengths $\lambda = 2\pi/k$ larger than the perimeter of the jet (or $\kappa = kr_0 < 1$) will have a negative change in energy and are thus unstable[6]. From this it is not yet clear though which will be the most unstable or fast growing mode.

A time dependence of the amplitude of the perturbations should thus be looked at. The perturbed cylinder can then instead of equation 2 be seen as

$$R(x,t) = R_0 + cos(kx)e^{\omega t} \qquad \text{[eq. 4]}$$

With R_0 the initial radius, k the wave number of the perturbations and ω the growth rate of the perturbations. The growth of the perturbations is what ultimately breaks up the jet. Using equation 4 in the equations of conservation will yield a dispersion relation for ω[5]

$$\omega^2 = -\frac{\gamma}{\rho R_0^3}(kR_0)[1-(kR_0)^2]\frac{I_1(kR_0)}{I_0(kR_0)} \qquad \text{[eq. 5]}$$

With γ the surface tension, ρ the density of the fluid, and I_1 and I_0 respectively the first and the zeroth order Bessel function.
Divided by k this yields

$$\frac{\omega^2}{k^2} = -\frac{\gamma}{k^2\rho R_0^3}(kR_0)[1-(kR_0)^2]\frac{I_1(kR_0)}{I_0(kR_0)} \qquad \text{[eq. 6]}$$

The growth rate of the perturbations thus depends on their wavelength. The most amplified wavenumber, called the Rayleigh mode, in the inviscid case is

$$kR_0 \approx 0{,}7 \qquad \text{[eq. 7]}$$

2.2 Capillary waves

From the derivation for the dispersion relation above can be concluded that for $0 < \kappa < 1$ ω becomes real, which will mean an unstable mode. When the perturbation wavelengths become sufficiently short, and $\kappa > 1$, equation 6 depicts an imaginary ω. Physically this means the waves will be traveling capillary waves.

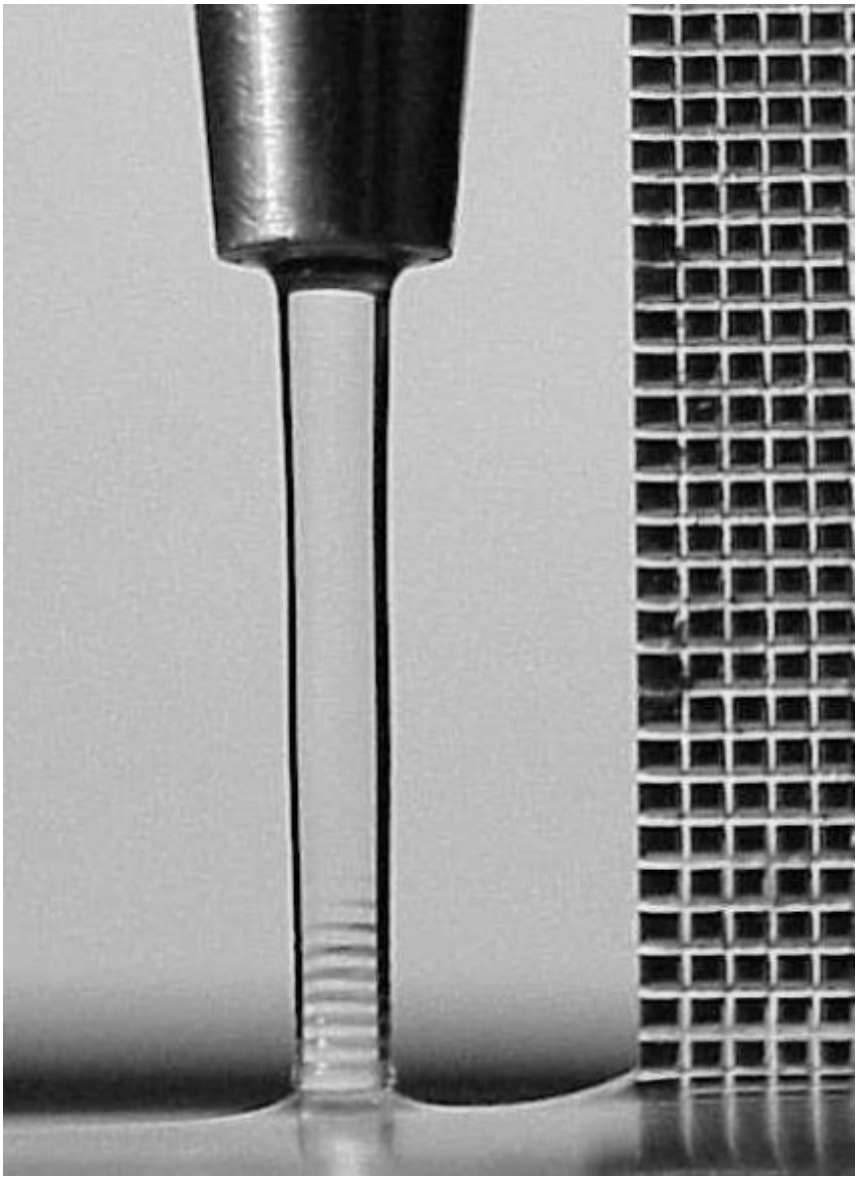

Figure 2: Jet impinging on a water reservoir. Capillary waves can be seen near the base of the jet, a millimeter grid can be seen on the right. [7]

In the case of a jet impinging on a water reservoir, like a steady stream of water from a tap falling into a sink filled with water, standing waves can be observed by the naked eye at the point where the jet impinges the water reservoir [fig. 2]. The standing waves are called

capillary waves. For the waves to be standing in the lab frame and also have a phase speed, the following condition must hold

$$\frac{\omega}{k} = -U_{cw} \qquad \text{[eq. 8]}$$

In which ω/k is the phase speed and u the local speed of the jet. This means that the waves move with the same speed but in opposite direction to the falling jet and thus appear to be standing in the lab frame. Combining equation 6 en 8 yields a relation between the wavenumber k and the speed of the jet

$$U_{cw}^2 = -\frac{\gamma}{\rho R_0^3}(kR_0)[1-(kR_0)^2]\frac{I_1(kR_0)}{I_0(kR_0)} \qquad \text{[eq. 9]}$$

From equation 9 and as noted assuming the phase speed of the capillary waves equals the jet speed, it follows that κ is constant, as is proven below.

Assuming

$$\lim_{kR_0 \to 0} \frac{I_1(kR_0)}{I_2(kR_0)} = \frac{kR_0}{2} \qquad \text{[eq. 10]}$$

And writing

$$t_{cap} = \sqrt{\frac{\rho R_0^3}{\gamma}} \qquad \text{[eq. 11]}$$

Which is called the capillary timescale.
With

$$U_{cap} = \frac{R_0}{t_{cap}} \qquad \text{[eq. 12]}$$

Where U_{cap} is the capillary speed which will be explained in more debt in the next section. Now equation 9 can be rewritten to

$$\frac{U_{cw}^2}{U_{cap}^2} = \frac{1}{2}(\kappa^2 - 1) \qquad \text{[eq. 13]}$$

With

$$\kappa = kR_0 \qquad \text{[eq. 14]}$$

Solving for κ

$$\kappa = \sqrt{1 + 2\frac{U_{cw}^2}{U_{cap}^2}} \qquad \text{[eq. 15]}$$

With $U_{cw}=U_{cap}$ this yields

$$\kappa = \sqrt{3} \qquad \text{[eq. 16]}$$

Which is the first approximation made for the dimensionless wavenumber. Thus when a jet falls into a reservoir with $U=U_{cap}$, $\kappa = \sqrt{3}$.

2.3 Tail drops

When the jet has pinched off from the jetting orifice and becomes free falling, a tail drop will form on the end of the liquid ligament. By drawing a control volume around the tail drop [fig. 3] it can be seen that the forces acting on the control volume are the line tension

$$F_{line} = -2\gamma\pi R_0 \qquad \text{[eq. 17]}$$

and the Laplace force which can be found by multiplying the Laplace pressure by the local area of the jet

$$F_{Laplace} = \frac{\gamma}{R_0}\pi R_0^2 = \gamma\pi R_0 \qquad \text{[eq. 18]}$$

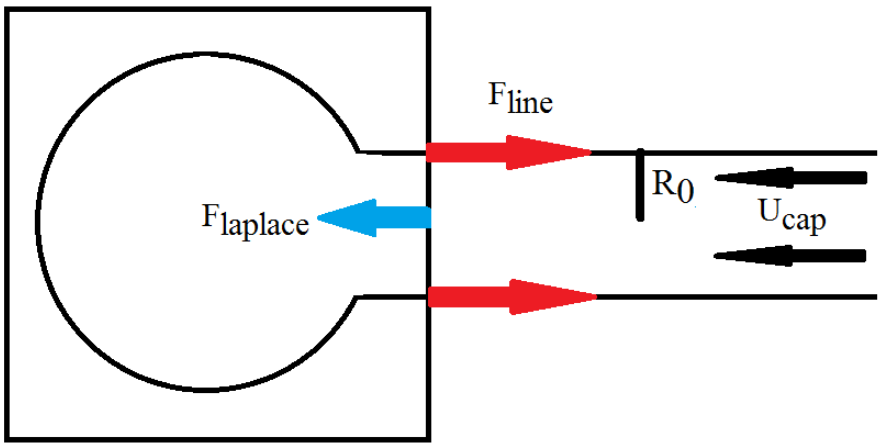

Figure 3: Control volume used to determine U_{cap}.

The tail drop will have a speed relative to the ligament which means stationary liquid will be added to the control volume which in turn means the tail drop will be slowed down. This process will result in the tail drop losing speed until its velocity is zero. This can be described by a momentum flux out of the control volume

$$\Phi_{momentum} = -u(\rho\pi R_0^2 u) \qquad \text{[eq. 19]}$$

If the tail drop does not pinch off from the ligament equilibrium between the momentum flux and the sum of the forces will occur

$$-\gamma\pi R_0 = -u(\rho\pi R_0^2 u) \qquad \text{[eq. 20]}$$

Solving this will yield an equilibrium speed called the capillary speed

$$U_{cap} = \sqrt{\frac{\gamma}{\rho R_0}} \qquad \text{[eq. 21]}$$

This capillary speed which was before set to equal the local jet speed can now be plugged into equation 15 which will lead to the second approximation for κ.

3 Experimental setup

When the tail drop moves into the liquid ligament at the capillary speed, the dimensionless wavenumber of the capillary waves is predicted to be $\sqrt{3}$. Both the velocity of the tail drop relative to the ligament and the wavelength of the capillary waves near the tail drop are determined experimentally.

3.1 Possible methods of capturing images of falling droplets

Capturing the droplets can be done in roughly two ways. The first approach uses a high speed camera to capture the droplets. The disadvantage of a high speed camera however is it low spatial resolution. The other way makes use of production of reproducible droplets and takes stroboscopic shots of these droplets. The latter requires a much more complicated setup in drop formation, but has a high spatial resolution. Furthermore the reproducibility enables the use of a regular camera, whereas the first method requires the use of a much more expensive high speed camera. With devices producing reproducible droplets available, keeping in mind reproducibility of droplets is a main target for the printing industry, the stroboscopic method is preferred in this experiment.

3.2 BNC pulse/delay generator

An integral part of the setup used in this experiment is a model 575 BNC pulse/delay generator (BNC). This apparatus connects all essential elements of the setup and arranges the timing of these elements in order for the setup as a whole to function properly. The actuation of the drop dispenser, the flash to illuminate the droplet and the shutter of the camera must be assigned in the right frame of time for any (useful) images to be captured.

The BNC is used to accurately delay the actuation pulse of the camera and the light flash with respect to the drop dispenser. This way images of later instances in time of the droplets are captured. By increasing this delay, a stroboscopic view of a set of droplets is created. To accurately control the BNC a Matlab algorithm called Lumenera is used. This algorithm assigns all initial settings (considering timing) necessary to the BNC and directly displays the resulting images captured by the camera.

The first step to capturing these images is to eject the droplets.

3.3 Microdrop dispenser

Indispensable for the stroboscopic approach is the reproducibility of the droplets. With a microdrop Technologies dispenser (microdrop) accuracies of $> 99\%$ can be attained[5]. A piezoelectric microdrop uses a capillary which is put under pressure by a piezo actuator. Piezo elements deform when a voltage is applied over the element. So by applying a voltage to a piezo element alongside the ink reservoir, the reservoir volume changes. A highly effective way to eject the fluid, in this experiment purified water, is called pull-push action or fill-before-fire action. In this method, before squeezing the liquid out, the reservoir is expanded, allowing more fluid to flow in. The pressure wave resulting from the expansion of the reservoir then reflects and becomes positive. This pressure wave then is amplified by the piezo element squeezing the reservoir and ejects the fluid from the nozzle. A more in depth study and comparisons between microdrop dispensers can be found in [9].

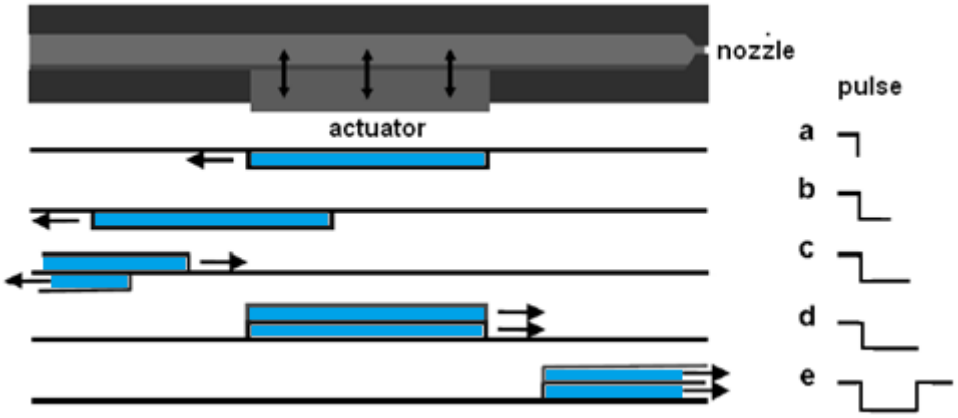

Figure 4: Stepwise ejection of fluid (displayed in blue) from a nozzle following a pulse input as displayed. (adapted from [10])

The pulses assigned by the BNC to the piezo elements are often not sufficient to eject droplets. Therefore an amplifier is needed, in this experiments a Krohn-Hite model 7602M wideband amplifier, to amplify the voltage to typically 90 - 130V. The exact amplification voltage is monitored with a Tektronix TDS 2014 oscilloscope.

The reservoir of the dispenser is connected to a much bigger reservoir with purified water. This reservoir is sealed and kept at a gauge pressure of -7 millibar to prevent the water from falling from the nozzle under influence of gravity. If this pressure is not applied, the

droplets wet the nozzle plate, which strongly decreases the reproducibility of the micro drops.

In this experiment a nozzle of 50µm in diameter is chosen. With all the criteria mentioned above met, droplets of approximately 1000 pl are produced. Next they must be illuminated to be able to capture their image with the camera.

3.4 iLIF

Illumination of the droplets is one of the key aspects in recording images of the droplets. In this experiment the light source is placed directly in front of the camera, with droplets falling between. The images captured therefore display the shadow of the droplets, rather than an image of the droplets.

In most studies a high performance LED is used as light source, because of their low cost. The resulting images however are rather susceptible to motion blur, as can be seen in figure 5. When an application only requires measurements on volume and speed of the droplets sharper pictures than these are not required. But when details of the droplets have to be studied they do not suffice.

Motion blur occurs when the exposure time of the camera is long enough for the object captured to displace in that frame of time.

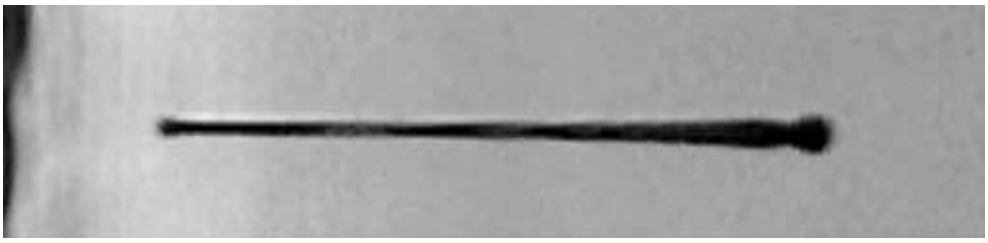

Figure 5: Image of a droplet captured with a LED as illumination displaying motion blur. [6]

Defining U as the speed of the object captured, the speed in pixels/s can be expressed by

$$U_{pix} = \frac{UM_{eff}}{d} \qquad \text{[eq. 22]}$$

With M_{eff} the effective magnification of the camera and d the pixel size in m/pixel. Defining ε the displacement of the object in pixels

$$\varepsilon = \frac{tUM_{eff}}{d} \qquad \text{[eq.23]}$$

A motion blur free image is captured when $\varepsilon < 1$. Therefore motion blur free images require an exposure time of

$$t < \frac{d}{UM_{eff}} \qquad \text{[eq. 24]}$$

In most cases of capturing droplet footage background light is negligible. Therefore the film can be kept exposed, waiting for the light flash to illuminate the film. The illumination time, rather than the exposure time, is now decisive for the amount of motion blur. Typical illumination time using a LED is in the order of microseconds, exceeding the time required for motion blur free images. With the use of a laser, this problem is avoided. Typical illumination times using lasers is in the order of nanoseconds (6 nanoseconds for the laser used in this study), sufficiently short to avoid motion blur, as can be seen in figure 6 below.

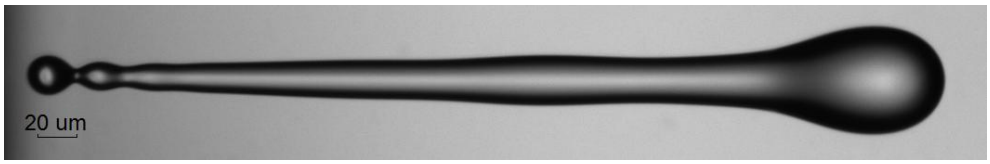

Figure 6: Motion blur free image captured using iLIF.

In general a downside of a short illumination time is low contrast in the image captured. Increasing the intensity of the light emitted increases contrast. A laser emits light of high intensity, therefore a laser still seems to be the best illumination source for stroboscopic imaging.

The high coherence of light emitted by a laser however introduces interference effects, resulting in fringes on the final image [fig. 7]. This is clearly unwanted. By illuminating a fluorescent plate with the laser light, non-coherent light is produced, removing the fringes. The intervention of a fluorescent plate does retard the light, increasing exposure time. Fortunately this retardation is too small, still in the range of nanoseconds, to introduce motion blur. The concept described above is known as iLIF (illumination by laser induced fluorescence).[1]

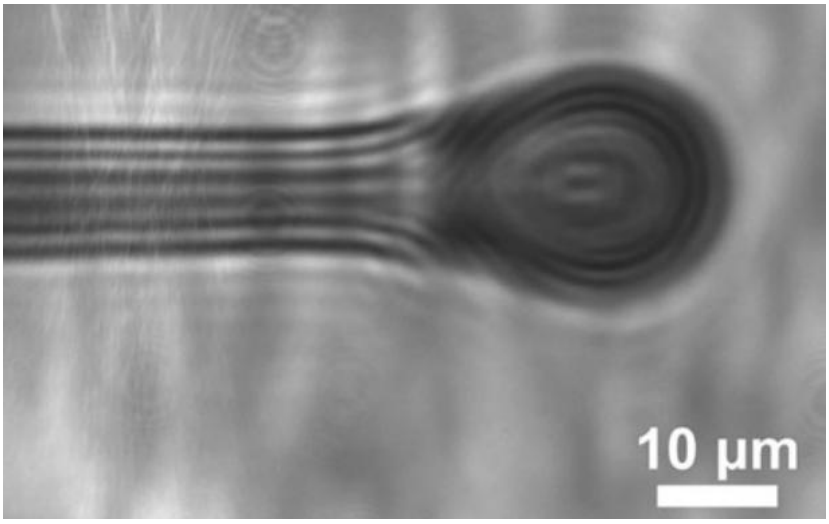

Figure 7: Fringes occurring using high coherent laser light as illumination, making the image useless for analysis.[1]

3.5 Camera and objective

In this experiment a Lumenera LW 135M-IO is used, a camera with a maximum frame rate of 15 frames per second. As mentioned in 3.1 the BNC actuates the shutter. The timing for this actuation can be done less accurately, since background light is negligible in comparison to the illuminating light pulse. Therefore the shutter time can be in the order of 60 microseconds, as only the nanosecond flash determines the exposure time of the film.

An objective is clearly necessary to be able to record the micro-droplets. The choice of objective is mainly guided by the Nyquist criterion. This criterion states that to avoid undersampling of the image at least two pixels must lie within the magnified spatial resolution r. In other words: $M_{eff} > 2d/r$. In this experiment a ten times objective is used, meeting the the Nyquist criterion. In figure 8 this objective can be seen.

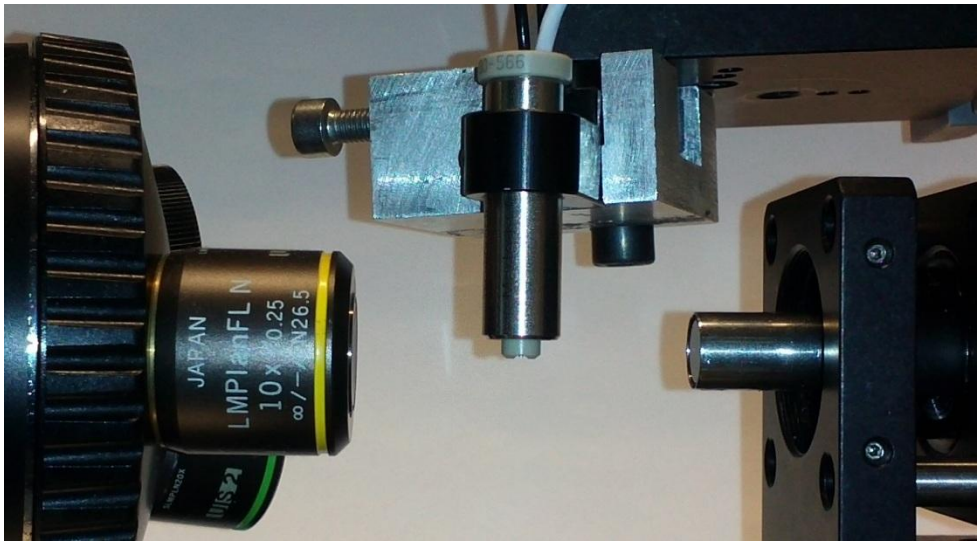

Figure 8: Experimental set-up of these experiments. Left: the objective. Center: the microdrop dispenser. Right: Optical fiber connected to the laser.

4 Analysis and results

The images captured with the camera are analyzed in MatLab with a number of algorithms. Firstly an algorithm determines the shape of the drop with an edge-routine. Several filters are available for this routine. The 'Canny' [11] method is accepted by different authors to be the most accurate filter [12] [13]. A result from the Canny edge determining method can be seen in figure 9. In general the Canny method works through the following steps: first a Gaussian filter smooths out the original picture to reduce desired image details. Then the gradient magnitude and direction of each pixel are determined. If the gradient of a pixel is higher than its next two neighbours in the gradient direction, the pixel is marked as an edge, otherwise it is marked as background. Finally weak edges are removed if they do not align with strong edges, this is called hysteresis thresholding.

Now with a second algorithm the edge of the drops can be analyzed further.

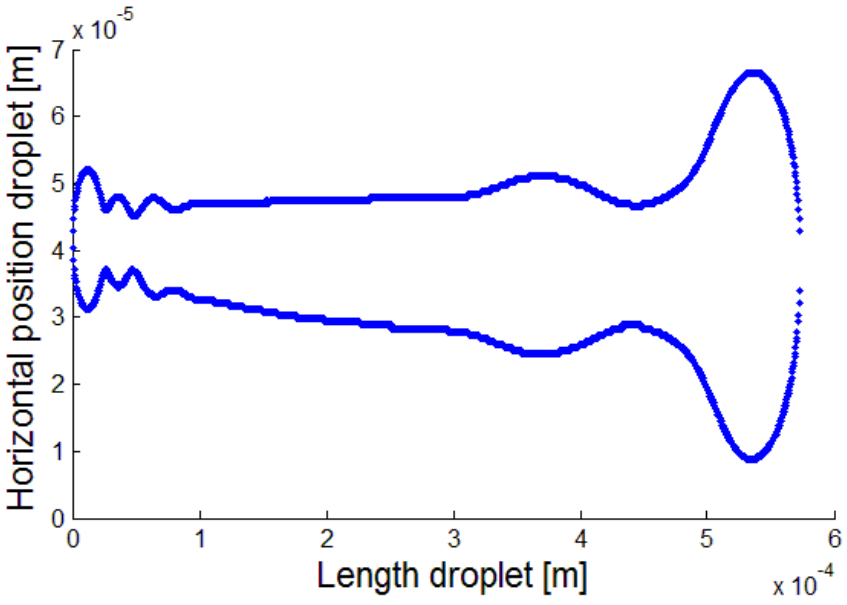

Figure 9: Trace of a drop made using the Canny method.

4.1 Dimensionless wavenumber

To find the dimensionless wavenumber of the capillary waves, the wavelength of the capillary waves and the radius of the ligament are determined. The dimensionless wavenumber then follows from

$$\kappa = \frac{2\pi R_0}{\lambda} \qquad \text{[eq. 25]}$$

In which κ is the dimensionless wavenumber, λ the wavelength and R_0 the local radius of the ligament.

The wavelength of the capillary waves is calculated by subtracting consecutive local maxima or local minima found in the trace. Another way of determining the wavelength would be a Fourier analysis of the tail drop. However only a small part of the liquid ligament is of interest in these experiments. Therefore Fourier analysis is not suitable in this case.

Because the edge routine does not produce a perfectly smooth and continuous curve but rather a more bumpy and pixelated function a lot of unwanted 'wavelengths' will be found. Luckily the bumps on the curve do generally not persist in time which means they will only show up as a single dot deviating from the curve on the final graphs of the dimensionless wavenumber against time. Apart from these unwanted 'wavelengths' a different kind of unwanted 'wavelengths' are produced with the subtracting method. An example of this can be found in figure 10. Wavelength B is unwanted - it does not contribute any useful data - but wavelength A should be kept. To achieve this, a low pass filter is first used to get rid of the longer wavelength. The cutoff length of the filter is determined by first plotting the full spectrum of wavelengths found by the algorithm and from there determining a suitable value which then can be incorporated in the script. The resulting wavelengths A are the capillary waves emitted by the tail drop.

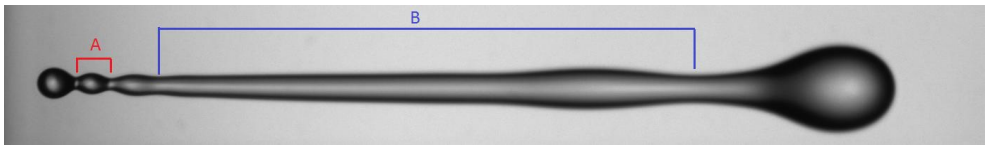

Figure 10: Distinction between useful (A) and undesirable wavelengths (B)

To determine R_0, firstly the volume of a single wavelength is determined with a Riemann sum over a series of discs one pixel wide and surface area $A=\pi r^2$. The radius of each disc is calculated by subtracting the local lower boundary of the edge from the local upper boundary. The boundaries of the Riemann sum are set as the first two local minimum on the ligament, wavelength A in figure 10.

$$V = \Delta x \sum_{0}^{\lambda} \pi r^2 \qquad \text{[eq. 26]}$$

The resulting volume is divided by the same wavelength, thereby treating the volume as a perfect cylinder.

$$A = \frac{V}{\lambda} \qquad \text{[eq. 27]}$$

The mean radius of the ligament R_0 is then determined by taking the square root of the disc area.

$$R_0 = \sqrt{\frac{A}{\pi}} \qquad \text{[eq. 28]}$$

Figure 10 below depicts this in a more visual way.

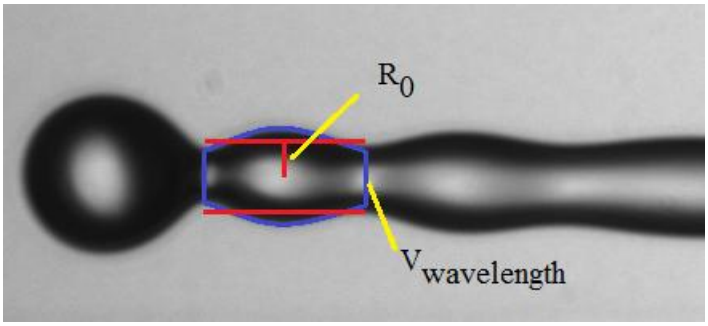

Figure 11: Determining the mean radius by treating the wavelength as a perfect cylinder.

The dimensionless wavenumber, κ, of the first two waves on the jet resulting from the experiments are plotted as functions of time. Start of measurement at t=0. Where t=0 is the moment the whole droplet has left the nozzle. Two different drops are analyzed here, the first [fig. 12] with a jetting voltage of 110 V and the second [fig. 13] with a higher jetting voltage of 118 V. As can be seen in the two figures the latter not only shows a lower value for kappa but also seems to have a shorter longevity. The second observation can be explained by breakup of the jet, or more specifically pinch off of the tail drop from the ligament occurring in an earlier stage when the liquid is jetted more forcefully from the orifice. The first observation will be discussed in more detail in the discussion in chapter 6.

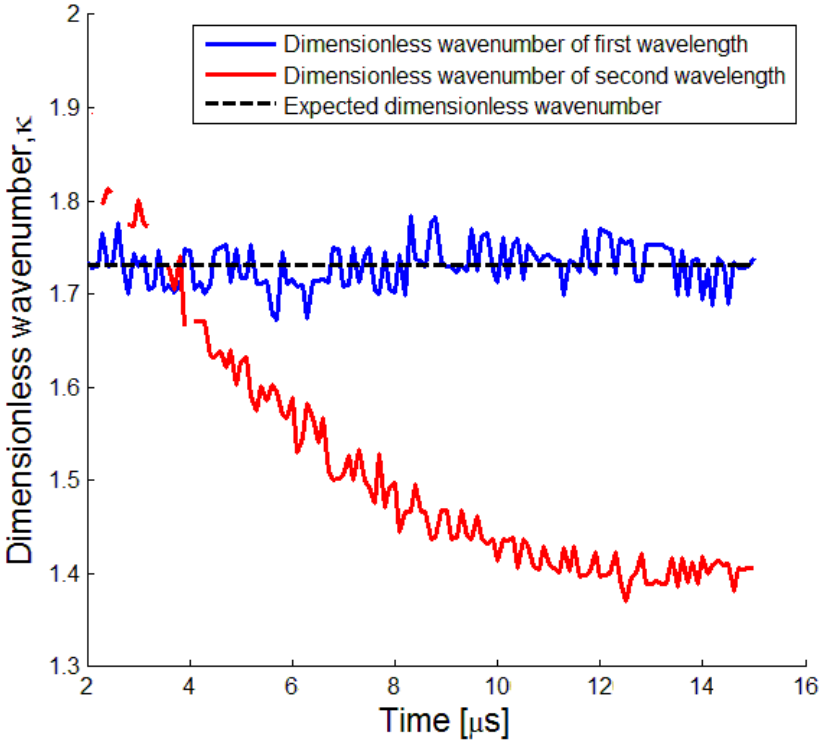

Figure 12: Dimensionless wavenumber of a drop ejected with a jetting voltage of 110 V.

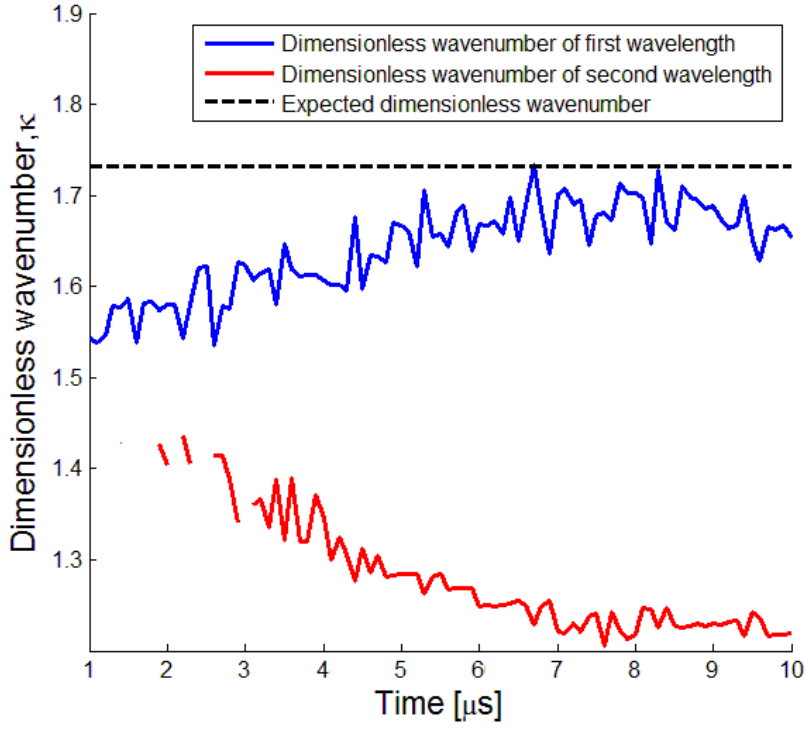

Figure 13: Dimensionless wavenumber of a drop ejected with a jetting voltage of 118 V.

The figures also show the expectation value $\kappa = \sqrt{3}$. Clearly the higher jetting voltage shows a bigger difference between the measured and expected value. Table 1 shows the mean deviation from $\sqrt{3}$ for a set of droplets at different jetting voltages. From this can be concluded that the higher jet speeds result in lower wavenumbers, or longer wavelengths.

Jetting Voltage (V)	Mean κ 1st wavelength	Mean deviation from $\sqrt{3}$ 1st wavelength in %	Mean κ 2nd wavelength	Mean deviation from $\sqrt{3}$ 2nd wavelength in %
110	1,73	0,5	1,59	8
112	1,71	1,5	1,57	10
114	1,72	1	1,55	11
116	1,67	3,5	1,49	14
118	1,64	5	1,28	26

Table 1: Deviation from expectation value $\kappa = \sqrt{3}$ of different measurements with different jetting voltages.

The functions for the second wavelength seems to be broken up between 10 and 30 (microseconds), this is because the wavelength has not been fully formed here.

4.2 Deviation from $U_{cw}/U_{cap}=1$

As stated in the theory a second approximation for the dimensionless wavenumber can be made by not setting $U_{cw}/U_{cap} = 1$, but by calculating U_{cw} as described in the following sections and using [eq. 21] to determine U_{cap}. The calculated U_{cw} and U_{cap} can then be plugged into equation 15 to find the dimensionless wavenumber.

Finding the local jet speed can be done by making the assumption that the speed of the capillary waves equals the relative speed of the tail drop with respect to the speed of the liquid jet. The relative speed of the tail drop then can be determined by measuring the growth rate of the tail drop. The influx of mass into the tail drop should equal the growth rate of the tail drop, as can be determined from figure 14.

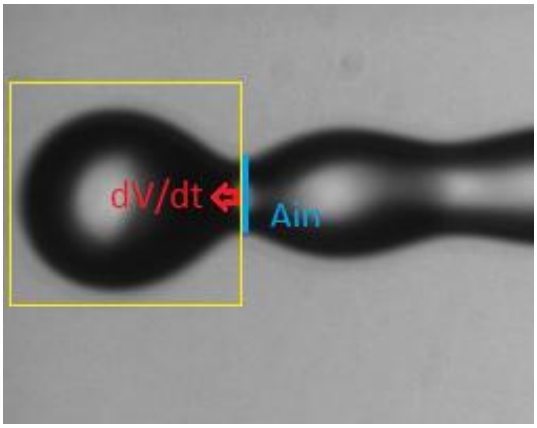

Figure 14: Control volume drawn to determine the relative speed of the tail drop.

Proof of the speed of the tail drop is in fact equal to the speed of the capillary waves is gained experimentally. The lower image in figure 15 is taken 7 μs, about four times T_{cap}, later than the upper image. Clearly the tail drop has increased in size, indicating that it moved relatively to the liquid. The distance between the tail drop and the capillary waves is kept intact, proving that the capillary waves move at the same speed as the tail drop.

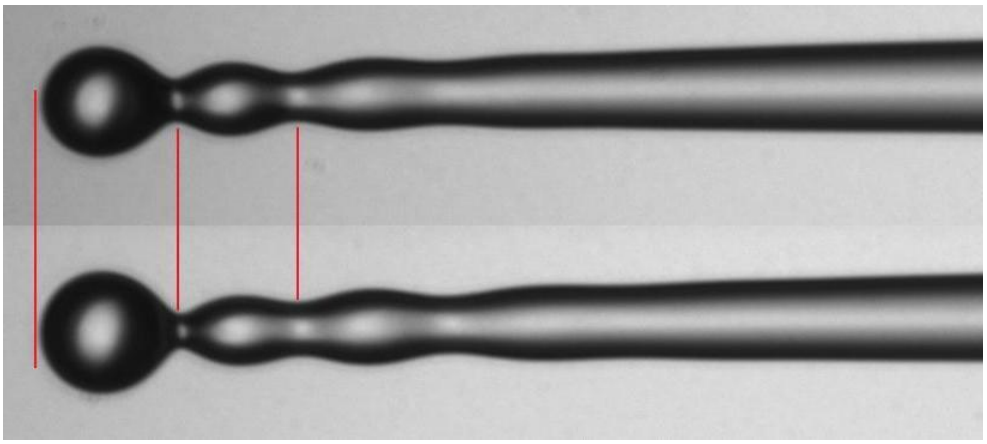

Figure 15: Example of the speed of the tail drop being equal to the speed of the capillary waves. Above: image of a drop captured at 5 μs. Below: image of a drop captured at 12 μs. This is a time frame of about four times of T_{cap}.

4.3 Growth rate of the tail drop

The volume of the tail drop is determined in the same way as was done in section 4.1. The boundaries for the Riemann sum are the same boundaries as chosen in the control volume in figure 14. The growth rate of the tail drop volume and thus the influx of mass into the tail drop can be determined by differentiation from a graph of time versus the tail drop volume.

$$\Phi_{vol} = \frac{dV_{td}}{dt} \qquad \text{[eq. 29]}$$

As can be seen in figure 15, the subsequent data points obtained from the measurements do not form a smooth curve. The graph suggests a growing function, growing linearly 'for the most part', but some data points deviate from this general outline. This means differentiation would result in a rather noisy curve. Therefore before differentiating the curve is smoothed by fitting a polynomial to the data points. A first order polynomial is fitted to the main, linear part of the curve, resulting in a constant growth rate. The result for the tail drop volume and the fit can be found in figure 16.

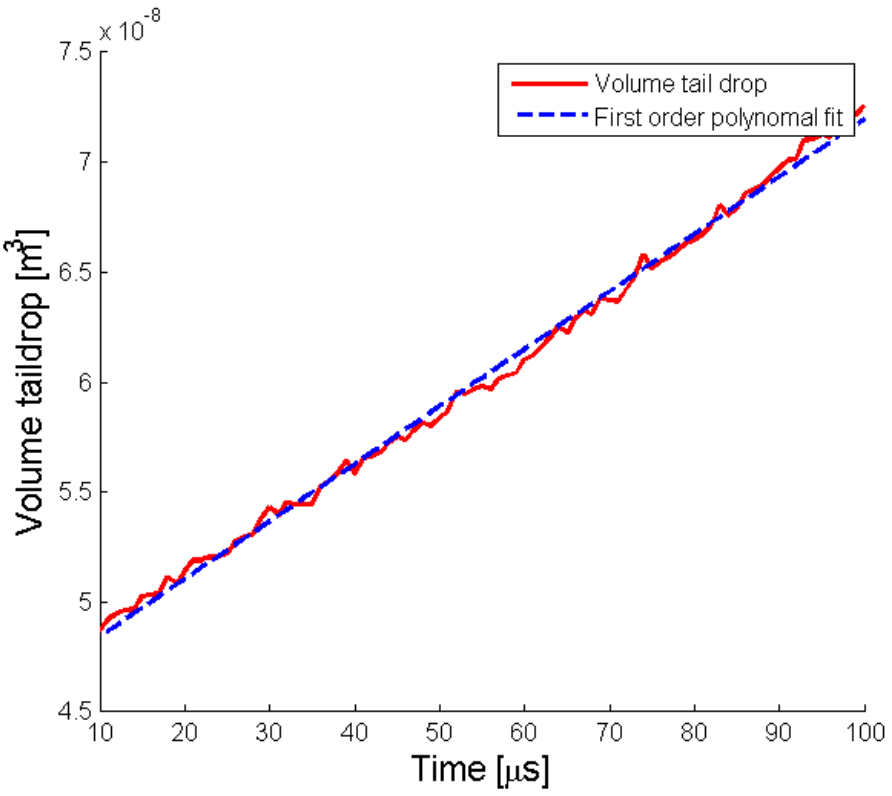

Figure 16: Fitted volume of a tail drop ejected with a jetting voltage of 118 V.

4.4 Relative speed of the tail drop

Dividing the growth rate by the area at the edge of the control volume now gives the relative speed of the tail drop.

$$U_{td} = \frac{\Phi_{vol}}{A_{in}} \qquad \text{[eq. 30]}$$

In the experiments A_{in} is found to change over time, as can be seen in figure 17, staying mostly constant and eventually decreasing until finally the tail drop pinches off from the jet.

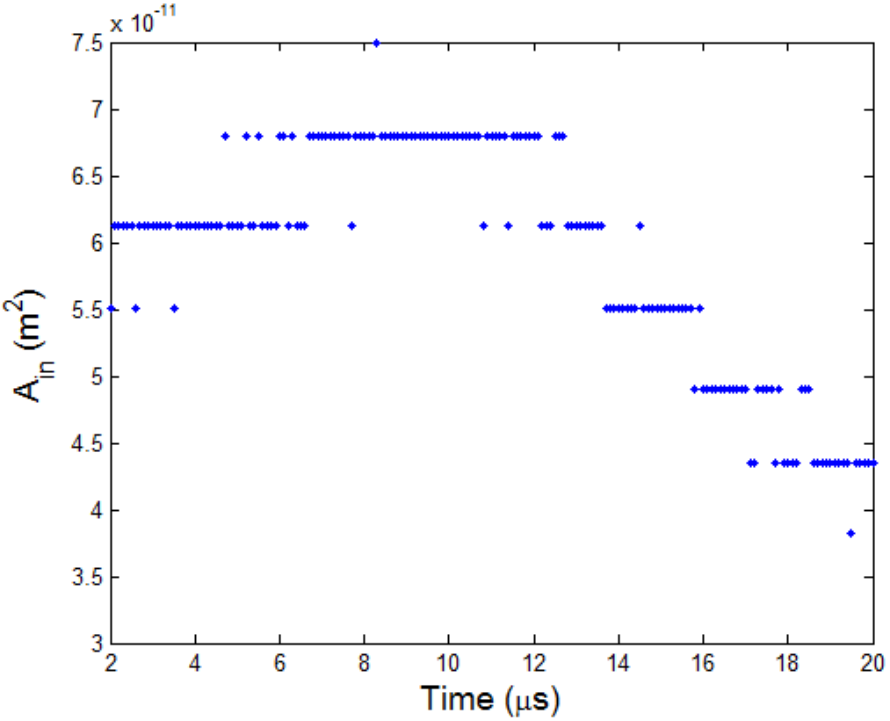

Figure 17: Change in area through which fluid enters the tail drop on a droplet ejected with a jetting voltage of 118 V.

4.5 Second derivation of dimensionless wavenumber

With both U_{cw} and U_{cap} known equation 15 can be plotted as a function of time as can be seen in figure 18 and 19. Clearly for both the low and high jetting voltage the theoretical dimensionless wavenumber deviates significantly more from the measured wavenumber. The expected wavenumber seems to be consistently higher than measured. This deviation is calculated for several measurements and shown in table 2.

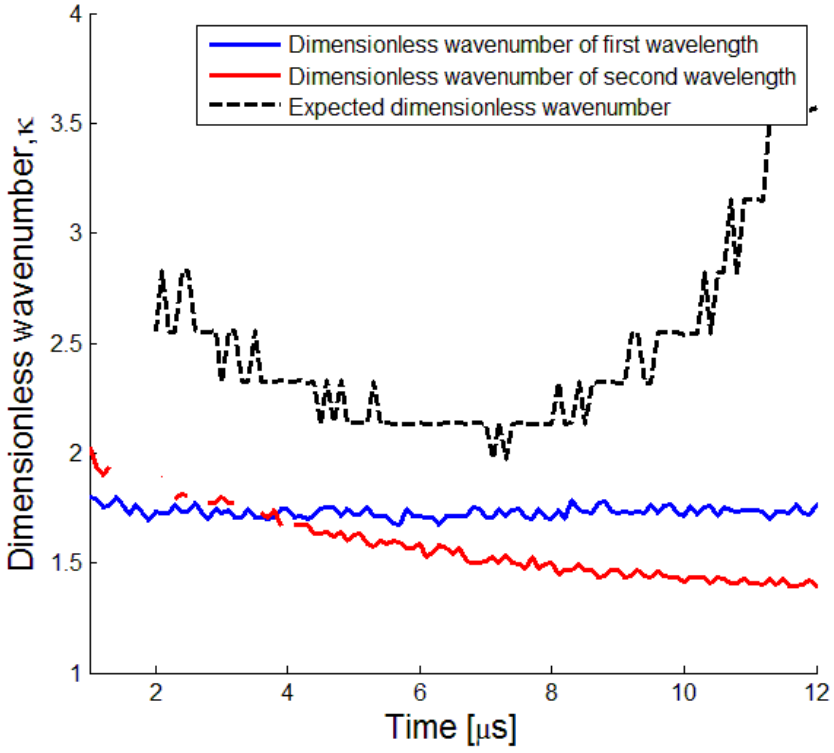

Figure 18: Dimensionless wavenumber for a droplet ejected with a jetting voltage of 110 V compared with a second approximation of κ.

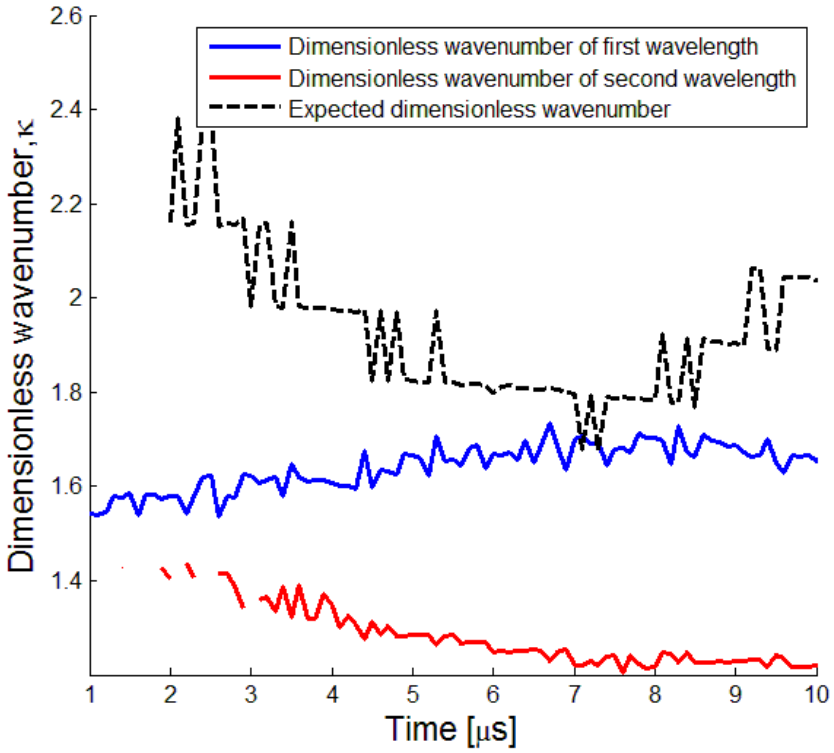

Figure 19: Dimensionless wavenumber for a droplet ejected with a jetting voltage of 118 V compared with a second approximation of κ.

Jetting Voltage (V)	Mean κ_2	Mean κ 1st wavelength	Mean deviation from κ_2 1st wavelength in %	Mean κ 2nd wavelength	Mean deviation from κ_2 2nd wavelength in %
110	1,99	1,73	13	1,59	20
112	1,99	1,71	14	1,57	21
114	1,97	1,72	13	1,55	21
117	1,91	1,67	14	1,49	23
118	1,92	1,64	17	1,28	33

Table 2: Deviation from the second approximation of the dimensionless wavenumber (κ_2) for different measurements with different jetting voltages.

5 Conclusions

The dimensionless wavenumber of capillary waves on liquid jets jetted with a microdrop dispenser with a jetting voltage of 110 V approaches the expectation value. For the drops jetted with a higher jetting voltage (for example 118 V), the dimensionless wavenumber decreases with increasing jetting voltage. A constant expectation value therefore does not agree with the measurements.

In the second approximation (dismissing the assumption $U_{cw}=U_{cap}$) the deviation of the measurements from the expectation value increases with respect to the deviation described in the paragraph above. This suggests that the theoretical model on which the expectation value is based is not applicable to these measurements. The agreement in the measurements using lower jetting voltages therefore seems either coincidental or a vital part in this simple approximation is missing.

Taking all of this into account it can be said that, despite a lot of remaining questions concerning the validity of the two approximations used, a better understanding of the dimensionless wavenumber of capillary waves emitted by tail drops on semi-infinite liquid jets evolving towards pinch off has been attained. It is clear that the tested models are far from complete and need to be improved significantly.

6 Discussion

The quantitative error in all measurements is in the order of 50-75%. This rather big error is mainly caused by the relatively low resolution of the camera used with respect to the small characteristic lengths in these experiments. Using such big error margins all measurements could be considered in agreement with the expectation value. It was decided not to draw this conclusion, since the measurements seem accurate enough to draw more specific conclusions. Therefore the error margins are not depicted in any figure either.

One of the main reasons the dimensionless wavenumber does not agree with the expectation value is the temporal instability of the droplets. In all experiments the correlation between the measured and expected value decreased rapidly when the droplet evolved towards pinch off of the tail droplet. This is somewhat circumvented by using only the stable parts of the droplet series.

In an earlier stage of these experiments the goal was to study pinch off phenomena. The shape and the stability of the drops were therefore subordinate to achieve pinch off. The drops captured thus are more suitable for analysis of pinch off than for analysis of the capillary waves in general. We were looking to produce droplets where pinch off was best achieved instead of making as stable droplets as possible.

In the second approach it is found that the ratio U_{cw}/U_{cap} exceeds 1, the value the theory prescribes. To agree with the theory therefore two solutions are possible: U_{cw} is measured too big or U_{cap} is too small. In our measurements and analysis we make some estimations in determining U_{td}, for example by fitting the growth rate with a first order polynomial. It might be possible important information was lost by fitting in this manner. This however does not seem to fully explain the discrepancy between measurements and theory and we see no signs of miscalculating U_{cw} in our analysis. This suggests that U_{cap} is estimated too small. This seems plausible, since the derivation of U_{cap} makes use of a fairly simple model of a perfect sphere and a perfect cylinder, whereas the drops created in these experiments show behaviour that is not simply explained with such a model. For example the radius of the undisturbed liquid jet R_0 is not constant.

This brings us to one of the most important disadvantages of finding an expectation value for these experiments: the phenomena surrounding pinch off are not that well understood. Therefore an accurate model describing U_{cap} is not available.

Although we can make no real founded statements where our approximations might go wrong, a fair guess would be the stretching of the liquid ligament over time. Seeing how the theory for the dimensionless wavenumbers is increasingly less accurate for higher jetting voltages and by taking into account the observation that the liquid ligaments seem to stretch out more and faster when the jetting voltage is increased, it is easy to see there might be a connection between the two.

A clear point of improvement is the use of a camera with a higher resolution to increase the accuracy in capturing the small characteristic lengths. The discrete steps seen in figure 17 are a good example of the low resolution used in these experiments. This increase in accuracy can also be achieved by using an objective with a higher magnification, but that would also mean the drop can only be partly recorded. This is undesirable when a bigger part of the drop is needed for analysis, such as analysis on stretching of the drop.

Another recommendation for further analysis is the use of a different filter for the edge-routine. When a sub-pixel filter is used, the local maxima and minima are defined more precisely and the discrete steps as in figure 16 should smoothen.

An error that may come forth from the setup is the way the jetting voltage is set. This is done with a highly sensitive turning knob, this can be easily improved by regulating this digitally.

A possible inaccuracy might occur in the assumption that all drops are reproducible. Observation during measurements however does suggest all drops are reproducible with only a small deviation. The inaccuracy in this therefore is negligible, especially considering the larger inaccuracy following the resolution of the camera used.

Acknowledgements

We would like to thank Mark-Jan van der Meulen and Theo Driessen for their help and guidance throughout the course of these experiments and for their constructive criticism and feedback on the earlier drafts of this thesis.

Also we would like to thank the research department Physics of Fluids for letting us use all the equipment needed to do these experiments.

References

[1] A. van der Bos, A. Zijlstra, E. Gelderblom and M. Versluis, *iLIF: illumination by Laser-Induced Fluorescence for single flash imaging on a nanoseconds timescale*, Experiments in Fluids, Vol. 51, Issue 5. p. 1283-1289, (2012)

[2] F.C. Krebs, *Fabrication and processing of polymer solar cells: A review of printing and coating techniques*, Solar Energy Materials & Solar Cells, Vol. 93, p. 394–412, (2009)

[3] Lord F.R.S. Rayleigh, *On the capillary Phenomena of Jets*, Proceedings of the Royal Society of London, Vol. 29, Issue 196-199, p. 71-97, (1879)

[4] J.A.F. Plateau, *Statique Expérimentale et Théorique des Liquides Soumis aux Seules Forces Molécularies*, Gauthier-Villars, (1873)

[5] C. Weber, *Zum Zerfall eines Flussigtkeitsstrahles*, Zeitschrift für Angewandte Mathematik und Mechanik, Vol. 11, Issue 2, p. 136–154, (1931)

[6] J, Eggers and E, Villermaux, *Physics of liquid jets*, Reports on Progress in Physics, Vol. 71, (2008)

[7] J.W.M. Bush, *MIT Lecture Notes on Surface Tension, lecture 5*, Massachusetts Institute of Technology, (2004)

[8] Microdrop Technologies microdrop dispenser manual

[9] E.R. Lee, *Microdrop Generation*, Chapter 2 Methods of Generating Monodispers Microdrops, CRC Press, Print ISBN: 978-0-8493-1559-6, (2002)

[10] H. Wijshoff, *Structure- and fluid-dynamics in piezo inkjet printheads*. Thesis, (2008)

[11] Ding, L., and A. Goshtasby, *On the Canny edge detector*, Pattern Recognition, Vol. 34, p. 721–725, (2012)

[12] M Juneja, P S Sandhu, *Performance Evaluation of Edge Detection Technique for Images in Spatial Domain*, International Journal of Computer Theory and Engineering, Vol. 1, Issue 5, (2009)

[13] R. Maini and H. Aggarwal, *Study and Comparsion of various Image Edge Detection Techniques*, International Journal of Image Processing, Vol. 3, Issue 1. (2009)